The influence of real gas effects on the performance of supercritical CO_2 dry gas seals

Z.M. Fairuz, Ingo Jahn

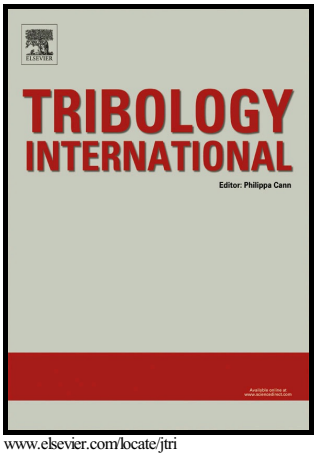

www.elsevier.com/locate/jtri

PII: S0301-679X(16)30140-2
DOI: http://dx.doi.org/10.1016/j.triboint.2016.05.038
Reference: JTRI4219

To appear in: *Tribiology International*

Received date: 17 February 2016
Revised date: 29 April 2016
Accepted date: 25 May 2016

Cite this article as: Z.M. Fairuz and Ingo Jahn, The influence of real gas effect on the performance of supercritical CO_2 dry gas seals, *Tribiology Internationa* http://dx.doi.org/10.1016/j.triboint.2016.05.038

The influence of real gas effects on the performance of supercritical CO_2 dry gas seals.

Z.M.Fairuz [a], Ingo Jahn [b]

[a] Queensland Geothermal Energy Centre of Excellence, School of Mechanical and Mining Engineering, The University of Queensland, 4072 St. Lucia, Queensland, Australia.
Email: zmfairuz@gmail.com

[b] Centre for Hypersonics, School of Mechanical and Mining Engineering, The University of Queensland, 4072 St. Lucia, Queensland, Australia.
Email: i.jahn@uq.edu.au

Abstract

The current work investigates dry gas seals operation with supercritical CO_2 (sCO_2) at two operating conditions using CFD. One close and one far from the critical point. At the operating condition far from the critical point a maximum change of 1.7% in pressure, 0.4% in temperature and 1.1% in density are observed. Contrary, closer to the critical point a maximum change of 6.5% in pressure, 6.7% in temperature and 39.5% in density are observed. These changes also influence opening force and leakage rate. Far from the critical point the maximum changes are 0.7% and 3.1%, whereas close to the critical point maximum changes of 3.4% and 10.3% are observed. The centrifugal effect plays an important role when operating with dense gases.

Keywords: Supercritical carbon Dioxside; Dry gas seal; real gas; Brayton cycle

NOMENCLATURE

a	flow factor
A	area, Helmholtz free energy,
F_o, F_c, F_p	opening force, centrifugal force and pressure force
h, h_g	film thickness or operating gap, groove depth
H	enthalpy
n	groove number
P	pressure
P_g	pressure at the end of the groove's wall
$\dot{m}$	leakage rate, mass flow rate
r, r_i , r_o	radius, inner and outer radius
Re_c, Re_p	radial Reynolds number, tangential Reynolds number
T	temperature
T_θ	friction torque or windage loss
U_r	velocity due to the moving frame, whirl velocity magnitude
V, V_r, U_r	absolute velocity, relative velocity and whirl velocity vectors
V_r	relative velocity magnitude
y	vertical distance to nearest wall

y^+	non-dimensional wall distance for a wall-bounded flow
Z	compressibility factor
α	spiral angle
β	ratio of groove to land
θ	angle
ℓ_l, ℓ_g	land arc length, groove arc length
μ	dynamic viscosity
ρ	density
τ	stress tensor
τ_w	wall shear stress
ϕ	flow coefficient, reduced Helmholtz free energy
ϕ^o, ϕ^r	flow coefficient for the ideal gas contribution
ω, $\boldsymbol{\omega}$	rotational speed, angular velocity vector

1. Introduction

Dry gas seals were introduced in the late 1960s [1]. The use of dry gas seals in high performance turbomachinery system as a new kind of noncontact mechanical seal, such as in centrifugal compressors, turbine, turbojet engines, turbofans has increased dramatically over the past 20 years, replacing traditional oil film seals in most applications [2,3]. A dry gas seal performs well in terms of less friction and wear, lower power consumption, lower leakage, longer service life, improved operational safety and rotor system stability as well as reliability compared to wet seal systems [1,4-11]. In other word, despite alternative sealing technologies being available and having been installed with varying degrees of success for certain applications, they are often limited in speed, operating conditions and pressure. Moreover, with changes in the operating condition, they are prone to problems such as high leakage and relatively short periods of operation [1,12]. Therefore, today dry gas seals are the preferred choice and are used in a wide variety of industries despite their increase mechanical complexity compared to other seal types.

Although many surface groove patterns have been developed, the spiral groove geometry is still the most widely used in mechanical seal applications today [6]. For many years, research and early performance analysis used narrow spiral groove theory, proposed by Vohr and Pan [7], Muijderman [13], Malanoski and Pan [14] and Smalley [15]. However, this theory only provides a one-dimensional solution, while ignoring the complicated geometrical boundary shape [8]. With the development of computers, more accurate numerical models have been employed to analyse performance characteristics. Numerical treatments based on the Reynolds equation that utilize the finite difference method, finite element method, and boundary element method have been employed [5,16]. Recently, Thatte and Zheng [9] used Reynolds equation for high pressure CO_2 compressible flow and implement an iterative solution procedure to solve the governing equations using Matlab. However, the solutions of the Reynolds equation supply only two-dimensional results.

The solutions of both the narrow spiral groove theory and the Reynolds equation are useful for performance estimations and preliminary designs, but are not accurate in elucidating the three dimensional flow dynamics in the gap between two seal faces [4]. Nor can it capture non-traditional velocity profiles that arise between the rotor and stator as a result of large centrifugal and inertia forces caused by the increased gas density [17,18]. Therefore Computational Fluid Dynamics (CFD), which incorporates real gas models is required to accurately predict the fluid behaviour in the dry gas seal operating with dense fluids such as supercritical CO_2.

Some studies are available in literature, which deal with three dimensional Reynolds Averaged Navier Stroke equation in elucidating the flow field in the gap between two seal faces using ideal gas

model [4,8,18,10,11]. Heshune et al. [8] investigate the distribution of the hydrodynamic gas film pressure, opening forces and leakage rate in the gap of the spiral grooved dry gas seals at different face clearances. Shahin et al. [10] studied gas seal performances using both spiral and different herringbone shape groove configurations at different rotational speed in forward and reverse rotation conditions. Jing et al. [19] studies the flow on spiral groove dry gas seal in the laminar and turbulent flow regime. Shahin et al. [11] performed studies with constant depth grooves and with different taper grooves. Bing et al. [4] used both direct numerical simulation (DNS) and Reynolds-averaged Navier-Stokes (RANS) to study the three dimensional flow dynamics in the spiral-groove dry gas seal. Hong et al. [6] performed comprehensive analysis to resolve the problem of simulating the complex conjugate heat transfer within the seal. While insightful, these works do not address performance with highly dense supercritical fluids.

The supercritical CO_2 Brayton cycle is being actively developed for potential application in a wide range of energy conversion applications [20,21]. Dry gas seal, once mature for operation with supercritical CO_2 have been recommended for these applications [21] as they are more reliable, cost efficient, safer and offer the lowest leakage of any type of seals that can be applied in the harsh supercritical CO_2 environment [1,12]. So far, no design guideline for dry gas seals are available for supercritical fluid Brayton Cycles [21,12]. One of the key challenges in designing a seal for this application are the highly non-linear fluid and thermodynamic behaviour of the working fluid within the dry gas seal. These can have a major influence on dry gas seal performance. New insight into fluid dynamics within these seals is required in order to design efficient and robust seals for operation with supercritical CO_2.

Furthermore, the studies in literature on the supercritical fluid dry gas seals are still missing a clear descriptions and characterization of how the real gas properties and high density of the supercritical fluid affect the performance and operability of dry gas seals at operating points typical for Brayton power cycle or any other turbomachinery application. The present work carries out a numerical investigation to understand how supercritical CO_2 influence performances of dry gas seals and to provide new insight into how to design dry gas seals for supercritical CO_2 sealing applications. Within the Brayton Cycle there are two possible sealing locations at either high or low operating temperatures [8,17] (turbine and compressor seals) where dry gas seal can be selected. Hence, the present study investigates two inlet conditions one close to the critical point and one far from the critical point. At both conditions, seals operating with CO_2 (real fluid) and air (ideal gas) are compared to highlight the differences.

2. Numerical model

This section describes the numerical model used to analyse the fluid mechanics in the dry gas seals operating with supercritical CO_2.

2.1 Fluid Governing Equations

The fluid is simulated using the Reynolds Averaged Navier Stokes (RANS) equations, applied to a rotating system. For the single rotating reference frame simulation, the governing equations based on relative velocity are given by:

- Mass conservation

$$\nabla \cdot (\rho V_r) = 0 \tag{1}$$

- Conservation of momentum

$$\nabla \cdot (\rho V_r V_r) + \rho(2\omega \times V_r + \omega \times \omega \times r) = -\nabla P + \nabla \cdot \tau \quad (2)$$

- Conservation of energy

$$\nabla \cdot (\rho H V_r) + \nabla \cdot \left(\rho \frac{1}{2} {V_r}^2 V_r\right) + \nabla \cdot \left(\rho \frac{1}{2} {U_r}^2 V_r\right) = k\nabla T + \nabla \cdot (\tau \cdot V_r) \quad (3)$$

where V_r is defined as:

$$V_r = V - U_r \quad (4)$$

$$U_r = \omega \times r \quad (5)$$

The numerical simulations are performed using the CFD package ANSYS Fluent version 16 [23].

2.2 Equation of state

Two equations of state are used for the simulations based on operating fluid and operating conditions. For ideal gas simulations the equation of state is:

$$P = \rho RT \quad (6)$$

For CO_2 simulations the Span and Wagner equation of state is employed with constants selected to suit real gas CO_2 . This equation of state has been selected due to its superior performance close to the critical point, where the accuracy is shown to be the same order as the uncertainty of experimental measurements [24]. The equation of state is interpreted as a fundamental equation in term of the Helmholtz energy A, in non-dimensional form given by [24]:

$$\frac{A(\rho, T)}{RT} = \phi(\delta, \tau) = \phi^o(\delta, \tau) + \phi^r(\delta, \tau) \quad (7)$$

For the CO_2 simulations the fluid property database REFPROP, released by NIST [25], is employed. This database is build on the Span and Wagner equation of state described above.

2.3 Flow factor

In practice fluid within the seal is subjected to shear driven and pressure driven flow. Therefore, the fluid flow is a combination of Couette flow in the tangential direction and Poiseuille flow in the radial direction. In order to determine fluid state more accurately, the flow factor, a is used based on work from Brunetiere et al. [26]. The fluid flow is turbulent for a >1 and laminar when a <1 [26, 19]. The flow factor a is calculated as [26]:

$$a = \sqrt{\left(\frac{Re_c}{1600}\right)^2 + \left(\frac{Re_p}{2300}\right)^2} \quad (8)$$

where Re_c and Re_p are the Reynolds number for the circumferential Couette flow and radial Poiseuille flow respectively:

$$Re_c = \frac{\rho \omega r h}{\mu} \quad (9)$$

$$Re_p = \frac{\rho V_r h}{\mu} \quad (10)$$

2.4 Computational grid and boundary conditions

Fig. 1a and b show the basic geometrical parameters of the spiral groove dry gas seal. The rotary ring contains grooves with a depth h_g, typically several micron in depth and rotates on its shaft. The dimensions and operating parameters are summarised in Table 1 and 2. The groove shape is based on a logarithmic spiral as shown in Fig. 1b, defined by [11]:

$$r = r_g e^{\theta \tan(\alpha)} \quad (11)$$

This shape ensures that at each point on the spiral curve the angle, α, between the moving direction and the tangent to the curve is the same.

The computational fluid domain used to stimulate the flow behaviour between the rotary and stationary wall of the dry gas seal is shown in Fig. 1c and d. The computational domain is magnified 1000 times in the axial direction to present the geometry and grid details. The computational grid is generated using the meshing tools e3prep and e3prepToFoam [29,30] to generate a parametrically defined structured multi-block hexahedral mesh. As shown in Fig. 1d the computational grid is more densely clustered near the inlet, groove end and outlet to properly capture the critical flow details in these regions.

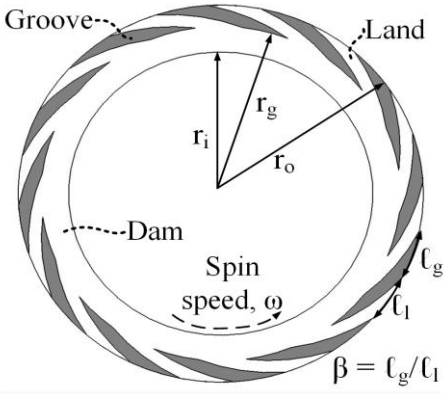

a) Schematic showning dry gas seal rotor.

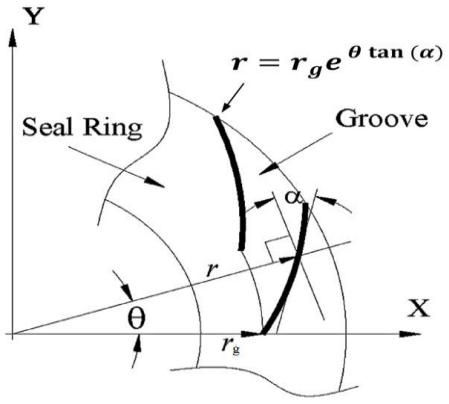

b) Definition of logarithmic groove shape.

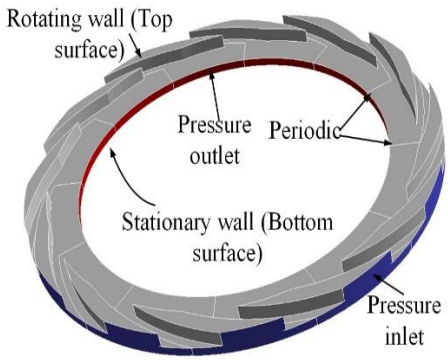

c) Enlarged fluid domain showing boundary conditions.

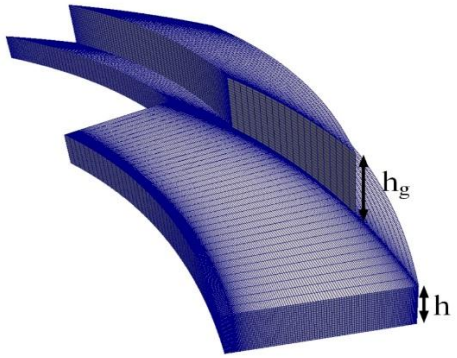

d) 1/12 segment of fluid domain used for simulation.

Fig. 1. Basic geometry parameters of the dry gas seal.

Table 1
Dry gas seal geometry.

Parameter	Value	
	Validation case [28]	Air and sCO_2 simulations
Inner radius, r_i (mm)	58.42	58.42
Outer radius, r_o(mm)	77.78	77.78
Groove root radius, r_g(mm)	69.0	69.0
Spiral angle, α (degree)	15	15
Ratio of groove to land, β	1	1
Groove number, n	12	12
Groove depth, h_g (μm)	5.0	5.0
Film thickness, h (μm)	3.05	3.05, 5.08 and 7

Table 2
Operation conditions.

Parameter	Value	
	Validation case [28]	Air and sCO_2 simulations
Inlet pressure, P_i (MPa)	4.5852	8.5
Outlet pressure, P_o (MPa)	0.1013	0.1013
Spin speed, ω (rpm)	10380	10380 and 30000
Fluid medium	Air	Air and CO_2
Operating temperature (K)	303	370 and 740
Fluid density at inlet for 370 K and 740 K (kg/m^3)	52.72	80.05 and 40.02 (Air) 155.43 and 60.48 (CO_2)
Wall temperature (K)	303	370 and 740

Operation conditions used for the present research are presented in Table 2. The pressure inlet and pressure outlet boundary conditions are used for inflow and outflow of the computational domain respectively. The non-slip boundary condition is employed at the wall. The single rotating frame method is used for mutual movement between the rotating and static seal ring. The isothermal temperature boundary condition is employed along the rotor and stator, with the assumption that rotor and stator are highly conductive and thus the generated friction heat is transferred out quickly so that the wall temperatures remains constant, a valid assumption as demonstrated by [18]. The rotating periodic boundary condition is used to simulate only one-twelfth of the whole fluid domain due to the geometrical similarity in circumferential direction to reduce computational cost.

The steady, compressible RANS equations are solved using an implicit, segregated, three-dimensional finite volume method. A second-order accurate, upwind discretization scheme is used for both momentum and energy equation. A pressure-velocity coupling is implemented with the SIMPLEC algorithm to solve the resulting algebraic equation system with the non-orthogonal correction to reduce the error due to the non-orthogonal meshes. The compressible ideal gas equation of state is used for air, whereas the REFPROP database is used for CO_2.

The shear stress transport (SST) k-ω turbulence model is used when solving the RANS equations. To properly capture the fluid flow close to the wall region, a mesh with the first cell height located at a $y^+ < 3$ is employed where y^+ it is defined as:

$$y^+ = \sqrt{\rho \tau_w}\, \frac{y}{\mu} \tag{12}$$

2.5 CFD validation and grid dependency study

To ensure the accuracy of the numerical model, a grid dependency study is conducted for four meshes, 'Very coarse' (0.15 millions), 'Coarse' (0.375 millions). 'Fine' (0.75 millions) and 'Very fine' (1.31 millions). Fig. 2 shows the pressure distribution along a line from the seal inner to outer edge (see appendix 1 for line definition) for air using both laminar governing equations and the k-ω SST turbulent model. It is observed that all meshes show comparable results. For air good agreement with the experimental data is also demonstrated. The maximum errors for peak pressure and total opening force are 2.6% and 5.59% respectively, as shown in Fig. 2a and b and summarised in Table 3. Hence, to save computational cost the 'Very coarse' mesh is used for further analysis. In addition, it is observed that the k-ω SST turbulent model has a better agreement in the groove region compared to the laminar flow as shown in Fig. 2a and b and Table 3 (P_g). This is in agreement with the flow factor a, which is 1.9539 even for h = 3.05 μm, suggesting that the flow in the seal is turbulent [26]. Therefore, the k-ω SST turbulent model is chosen for the current simulation.

A grid sensitivity study was also conducted for CO_2 operating near the critical point (T = 370 K, P_i = 8.5 MPa, ω = 30000 rpm) at 3μm film gap where the pumping effect is most intense. Fig. 2c shows the comparison of pressure traces for the CO_2 simulation. Again mesh independence exists for all meshes, justifying the use of the 'Very coarse' mesh for further simulations.

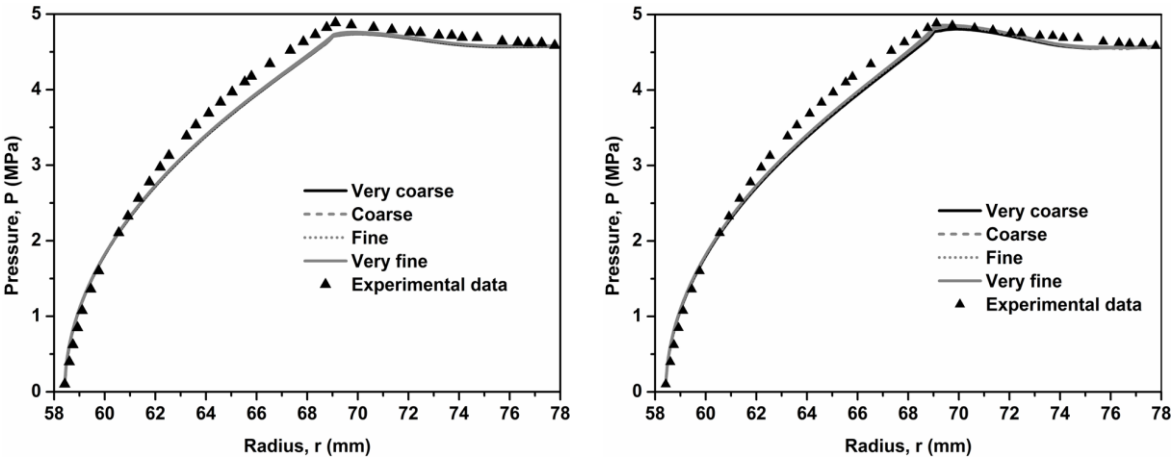

a)
Seal operating with air (ideal gas equation of state), laminar flow model.

b)
Seal operating with air (ideal gas equation of state), k-ω SST turbulence model.

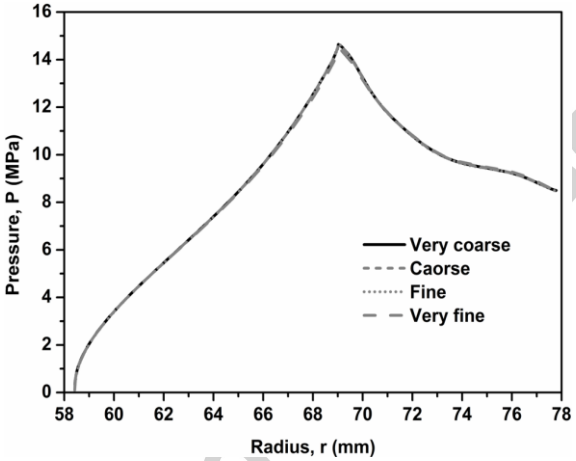

c)
Seal operating with CO_2 (Span and Wagner equation of state), k-ω SST turbulence model.

Fig. 2. Pressure distribution in radial direction for turbulence and laminar models and different mesh refinements, h = 3.05 μm.

Table 3
The comparison laminar and turbulent results to experimental data [28] for air.

Cases	Film gap, h (μm)	Groove Pressure, P_g (MPa)	ΔP_g (%)	Opening force F_o (N)	ΔF_o (%)
Laminar	3.05	4.70339	2.62	31367.0304	5.43
k-ω SST	3.05	4.81562	0.30	31315.3092	5.59

The higher discrepancy around groove region to the experimental data can be attributed to the non-uniform pressure distribution in the circumferential direction as shown in Fig. 3. In addition, differences in geometry at the inner end of the groove wall, sharp edged in the simulation and round edged in the experiment due to fabrication limitations, is a likely further contributor to the observed pressure discrepancy.

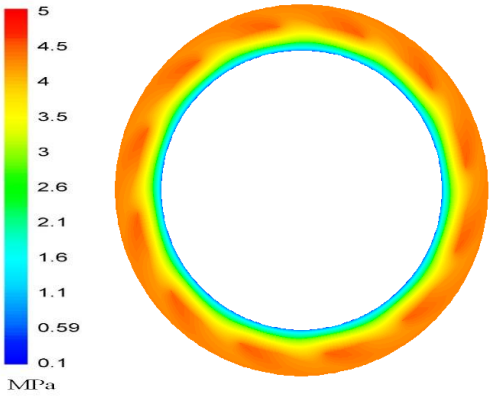

Fig. 3. Pressure distributions of air (ideal gas equation of state) for k-ω SST turbulent model, h = 3.05 μm.

3.0 Results and discussions

CO_2 experiences significant real gas effects when operating near the critical point. In dry gas seals the resulting non-linear variations in properties can change the performance. To explore these effects, two operating points with inlet conditions, close and far from the critical point are selected. First, different equations of states are used in order to quantify the influence of CO_2 real gas effects on seal performances. Then, a like-for-like comparison is performed to compare operation with air (ideal gas) and CO_2 (real gas).

3.1 Comparison of ideal gas and real gas CO_2 operation

Before conducting detailed investigation on the performance of the supercritical fluid dry gas seal, it is important to establish an understanding of how the real CO_2 gas properties near and far from the critical point affect seal operation compare to an ideal gas. The supercritical region is defined by operating pressure and temperature above the critical point P_{cr} = 7.4 MPa and T_{cr} = 304 K for CO_2 [22]. To characterised this behaviour the supercritical CO_2 seal described in Table 2 is investigated at two operating temperatures: i) T = 370 K for operation close to the critical and ii) T = 740 K for operation far from the critical point. In the following results, the performance of a seal simulated using the perfect gas law (Eq. (6)) with appropriate constants for CO_2 are compared to simulations using the Span and Wagner equation of state (Eq. (7)).

3.1.2 Pressure

Fig. 4 and 5 show the pressure distributions at rotational speeds 10380 and 30000 rpm respectively. Close to the critical point as shown in Fig. 4a and 5a, the pressure is up to 4.8% and 6.5% higher in the real gas simulation, especially near the end of the groove. On the contrary far from the critical point the pressure only shows a slight change of 1.3% and 1.7% (Fig. 4b and 5b). As expected the difference between the two equation of state increases as we get closer to the critical point. Furthermore, as the rotational speed increases, due to the more intense shear action that results in stronger outward pumping of the fluid in the groove, the deviation is further amplified in the high speed case, especially near the end of the groove where the highest pressure and thus most intense

fluid property changes are developed. As will be shown in section 3.2.2, the difference in pressure for the 370 K condition is mainly caused by differences in density between the two equations of states. The higher density predicted by the real gas equation of state can lead to higher centrifugal forces that enhance groove efficiency.

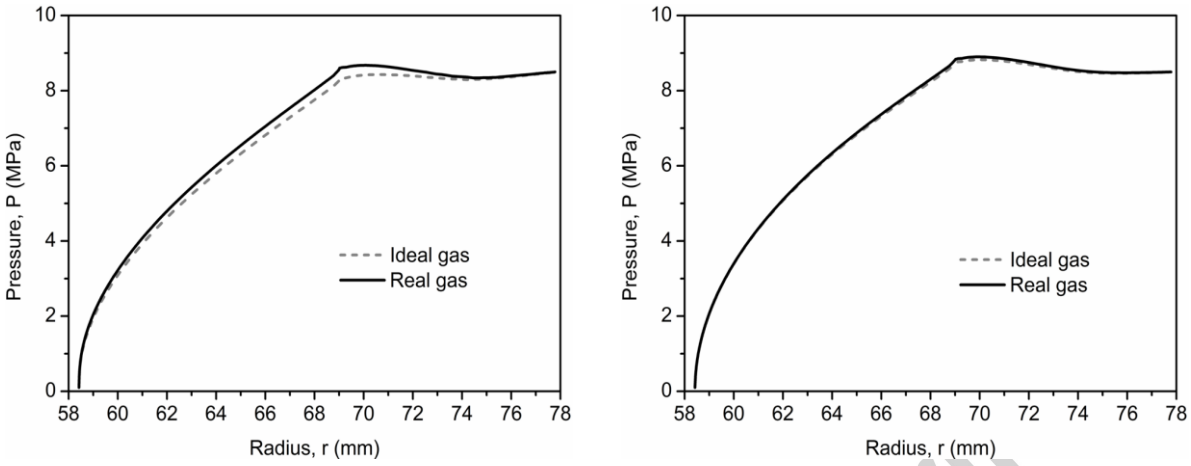

(a) T = 370 K (b) T = 740 K.

Fig. 4. Pressure distribution of CO_2 for ideal and real gas in radial direction, ω = 10 380 rpm and h = 3.05 µm.

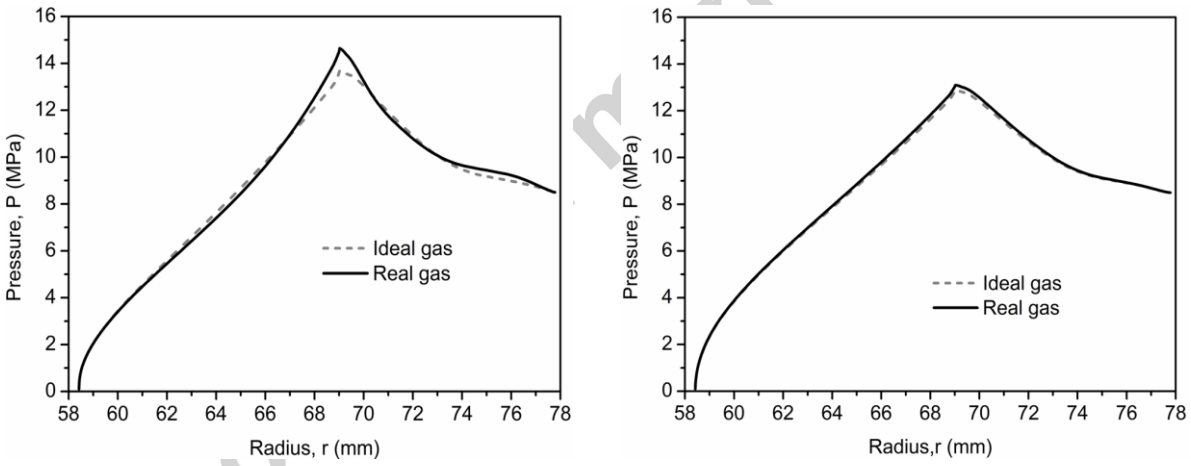

(a) T = 370 K (b) T = 740 K

Fig. 5. Pressure distribution of CO_2 for ideal and real gas in radial direction, ω = 30 000 rpm and h = 3.05 µm.

3.1.3 Temperature

Similarly, the temperature distributions also show a deviation between the two equations of state, particularly close to the critical point (Fig. 6a and 7a) with maximum differences of 4.6% and 6.7% for rotational speeds of 10380 rpm and 30000 rpm respectively close to inner edge. However, at the low rotation speed, the higher discrepancy is observed close to inner edge whereas at high rotation speed, the higher discrepancy is observed throughout the seal domain. On the contrary at high

temperature, far from critical point only minimal changes of 0.02% and 0.4% are observed for rotational speeds of 10380 rpm and 30000 rpm respectively (Fig. 6b and 7b). As evident from Figs. 6 and 7, the maximum deviation from and isothermal fluid temperature within the seal gap occurs for Fig. 6 and especially Fig. 6(a). This is attributed to an increasing tangential flow Mach number. At higher Mach number (high rotor speed and low temperature) energy dissipation is no longer negligible.

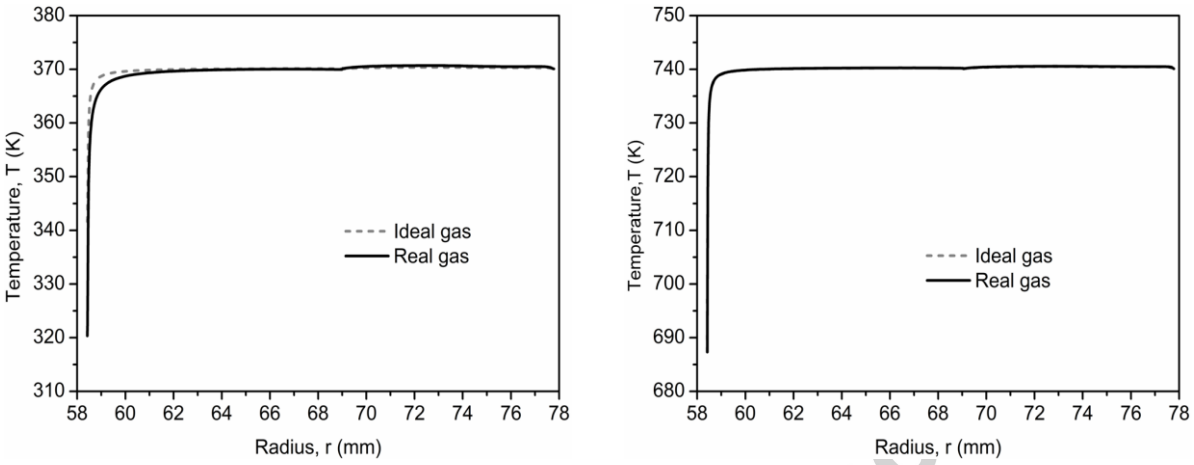

a) T = 370 K b) T = 740 K

Fig. 6. Temperature distribution of CO_2 for ideal and real gas in radial direction, ω = 10380 rpm and h = 3.05 μm.

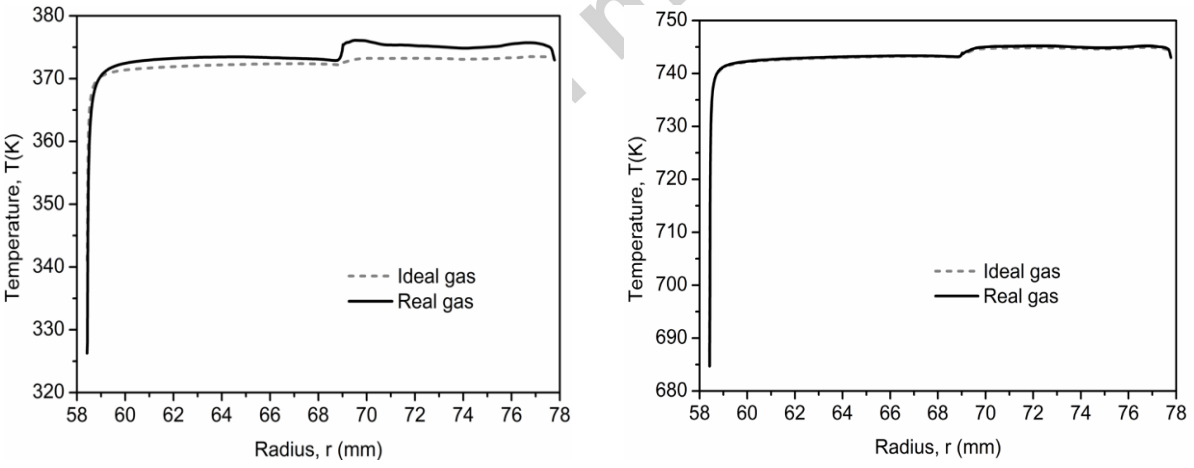

a) T = 370 K b) T = 740 K

Fig. 7. Temperature distribution of CO_2 for ideal and real gas in radial direction, ω = 30000 rpm and h = 3.05 μm.

3.1.4 Density

The radial density distributions are shown in Fig. 8 and Fig. 9. As expected due to the less significant real gas effect far from the critical point at T = 740 K, the results for ideal and real gas equations of state are almost identical with differences of 1.0% and 1.1% for rotational speeds of

10380 rpm and 30000 rpm respectively. On the contrary, a significant density difference is observed close to the critical point with 370 K inlet temperature. Differences of 24.8% and 39.5% are observed for rotational speeds of 10380 rpm and 30000 rpm respectively, with differences growing as the absolute pressure increases. This is due the different equations of state (i.e. Eq. (6) and Eq. (7)). Close to the critical point, these return substantially different density values for a given state point.

This indicates that the ideal gas law is not accurate in predicting the fluid and thermodynamic properties of the CO_2 when fluid conditions at the seal inlet, outlet, or within the seal are in the proximity of the critical point. Thus the Span and Wagner equation of state is highly recommended for the simulation of supercritical CO_2 dry gas seal when operating conditions are close to the critical point.

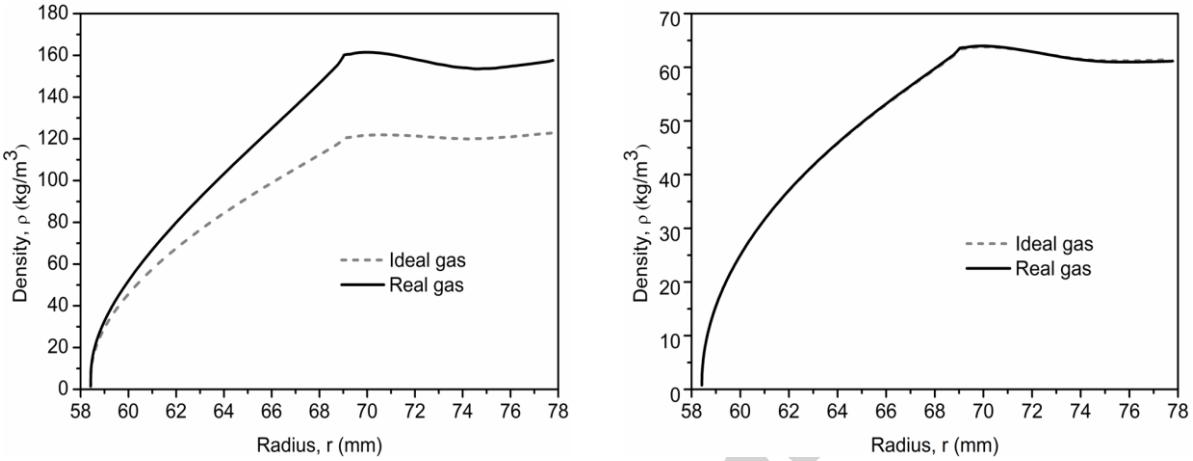

a) T = 370 K b) T = 740 K

Fig. 8. Density distribution of CO_2 for ideal and real gas in radial direction, ω = 10380 rpm and h = 3.05 µm.

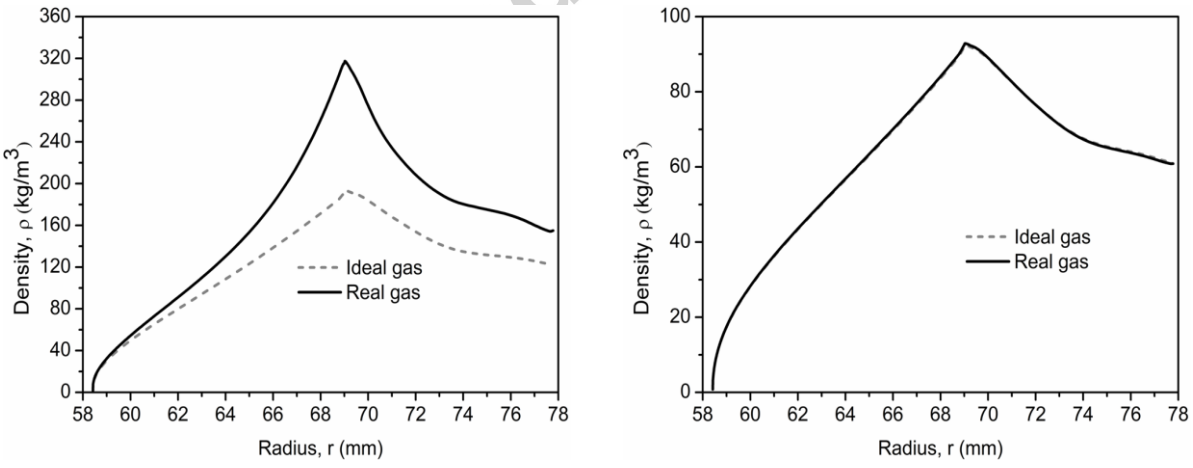

a) T = 370 K b) T = 740 K

Fig. 9. Density distribution of CO_2 for ideal and real gas in radial direction, ω = 30000 rpm and h = 3.05 µm.

Hence, the fluid and thermodynamic properties (Fig. 4 – Fig. 9) of the supercritical fluid show

that close to critical point, the real gas effect is significant and that the ideal gas law assumptions is no longer valid whereas far from critical point the supercritical fluid can be approximated by an ideal gas without loss of accuracy. This observation is confirmed by the compressibility factor discussed next.

3.1.5 Compressibility factor

The compressibility factor, Z also known as compression factor can be interpreted as the measure of fluid's deviation from ideal gas law [28].

$$Z = \frac{P}{\rho RT} \tag{13}$$

For ideal gas, the compressibility factor is close to unity [22, 27].

Fig. 10 and 11 show contours of compressibility factor for operation near and far from the critical point. With an inlet temperature of 370 K, close to the critical point the compressibility factor, Z is no longer close to unity as shown in Fig. 10a and 11a. This explains the high deviations from the ideal gas law shown in Fig. 4a - 9a. Especially in the groove region, where multiple factors interact to generate the highest pressures, these deviations from the ideal gas behaviour is significant. On the contrary, far from the critical point shown in Fig. 10b and Fig. 11b, the supercritical fluid behaves like an ideal gas as previously shown in Fig. 4b - 9b.

This confirms that near the critical point the ideal gas approximation is no longer valid.

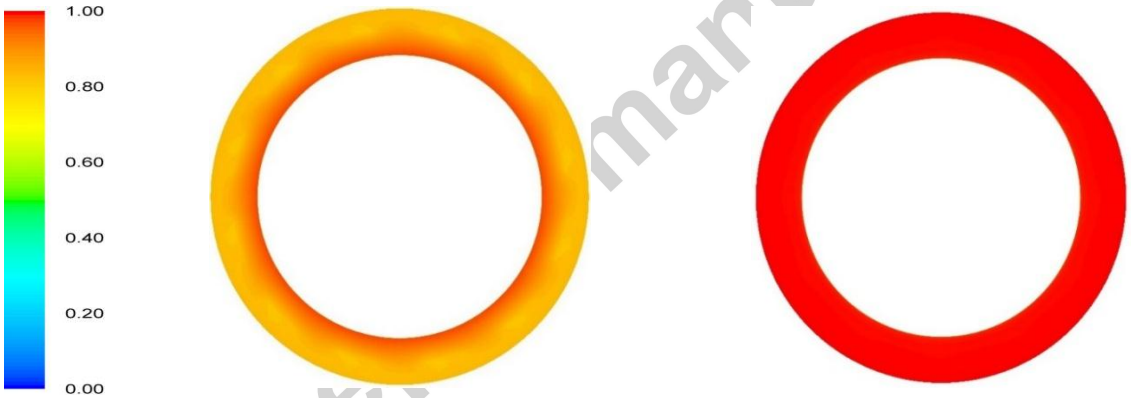

a) T = 370 K b) T = 740 K

Fig. 10. Contours of compressibility factor, Z at ω = 10380 rpm.

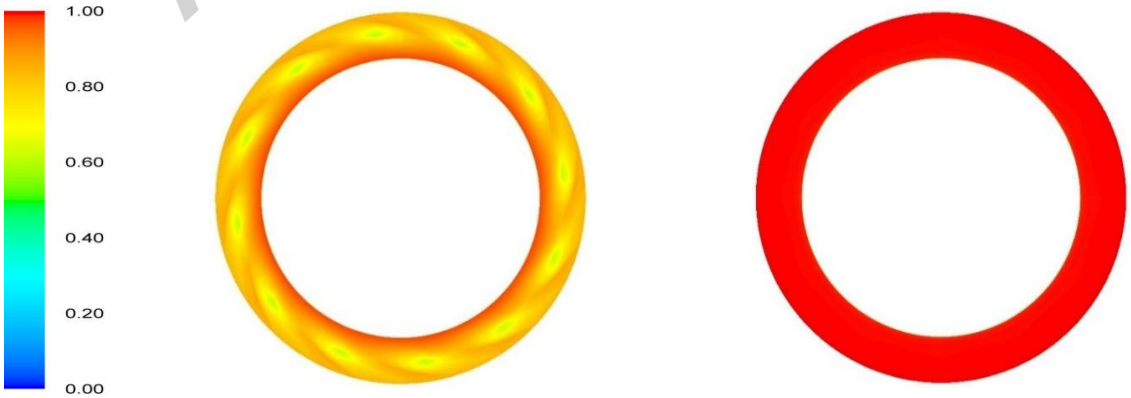

a) T = 370 K b) T = 740 K

Fig. 11. Contours of compressibility factor, Z at ω = 30000 rpm.

3.1.6 Performances of ideal and real gas of CO_2

Fig. 12 and 13 compare the seal performance and how this is affected by the selected equation of state. Seal performance is compared in term of opening force and outflow leakage rate. The opening force is the total seal opening force acting on the stator, calculated as:

$$F_o = \int p \, dA \tag{14}$$

Consistent with the comparison of underlying effects, a higher discrepancies is observed near the critical point. Close to the critical point the difference in opening force is 1.4% and 3.4%, for ω = 10380 rpm and ω = 30000 rpm, whereas far from the critical point the differences is only 0.2% and 0.7 % respectively. In all cases the real gas equation of state predicts a higher opening force. This is most likely caused by the predicted higher densities (see Fig. 8 and 9), which enhance the magnitude of the peak pressure that develops [18].

For leakage rate, near the critical point the real gas equation of state predicts a 8.1% and 10.3% higher leakage, whereas far from the critical point it predicts a lower leakage by 3.1% and 2.8% for ω = 10380 rpm and ω = 30000 rpm respectively. The higher leakage for the real gas equation of state close to the critical point can be attributed to the combined effect of increased density and peak pressure generated by the groove, both of which are detrimental to the performance of the sealing dam.

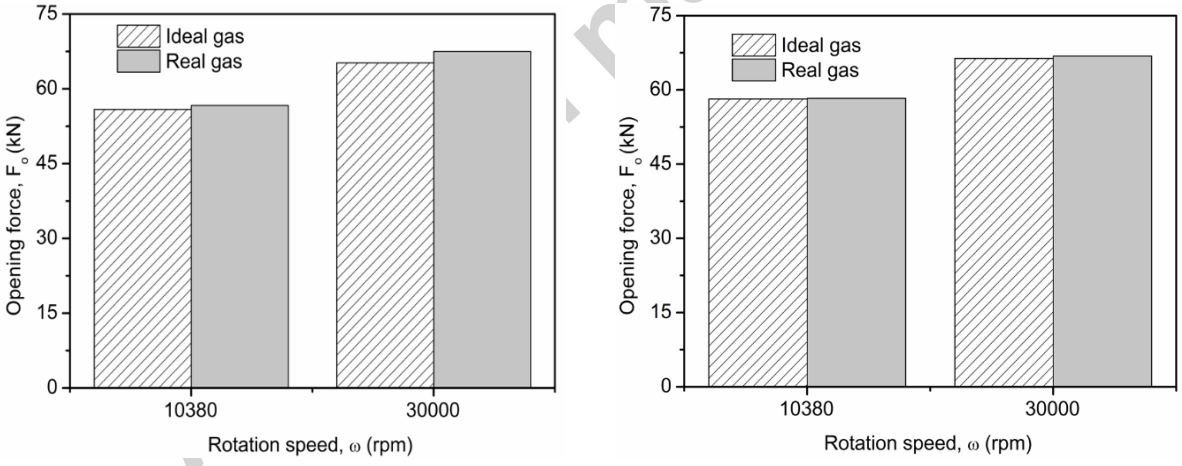

a) T = 370 K b) T = 740 K

Fig. 12. Opening force, F_o of CO_2 at different rotation speed for ideal and real gas.

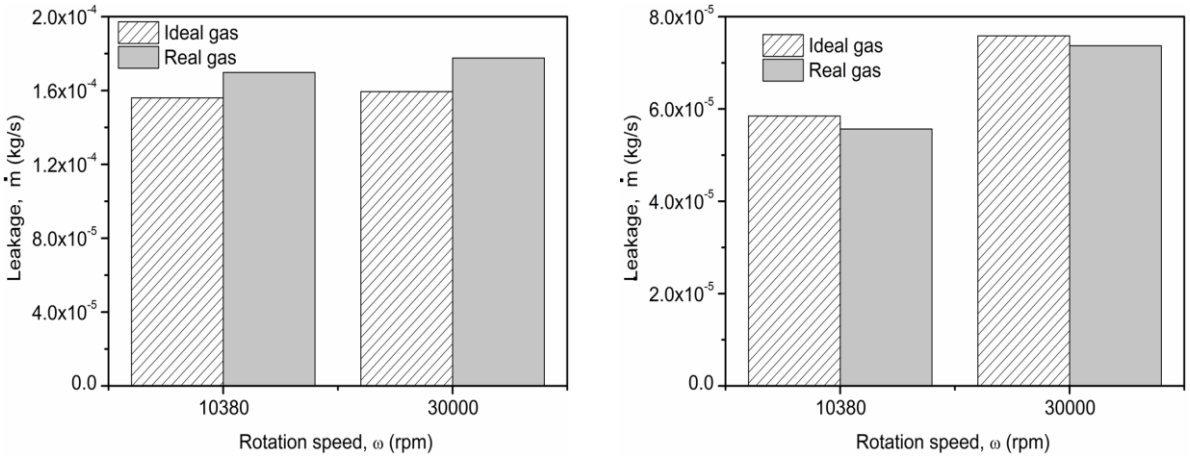

a) T = 370 K b)T = 740 K

Fig. 13. Mass flow rate, ṁ of CO_2 at different rotation speed for ideal and real gas.

Overall, when operating with CO_2, real gas effects can have a significant effect on fluid properties within the seal, particularly density. Significant differences exist between the results of the real gas and ideal gas simulations. This indicates a significant real gas effect when operating with CO_2 and highlights the need to use an appropriate equation of state. This observation is confirmed by the comparison of seal operation with air and supercritical CO_2 discussed next.

3.2 Comparison of seal operation with air and supercritical CO_2

To create further insight for seal operation with supercritical CO_2, this section compares the operation of two identical seals operating with air and supercritical CO_2 respectively. The seal operating conditions are given in Table 3. At these conditions the air seal acts as a reference point whereas the CO_2 exemplifies the effects of supercritical fluids and the associated non-linear real gas properties. In addition the CO_2 seal operates with the high densities typical for supercritical working fluids (see Table 2). The study considers three seal opening gaps, 3.05 µm, 5.08 µm and 7 µm.

3.2.1 Pressure distribution in sealing dam

As shown previously significant pressure peaks are attained at the end of the grooves. To understand this phenomenon, the balance of mass-flow between the fluid entering the groove and the flow leaving the groove toward the dam region must be considered.

In the dam region the fluid is influenced by two main factors in the radial direction; the pressure gradient and the centrifugal effect. In this work, in general the pressure gradient causes the fluid to flow inwards, while the centrifugal effect acts in the opposite direction. Particularly close to the rotor, where tangential velocities are highest substantial radial forces exist, which can cause the fluid to overcome the radial pressure gradient and flow outwards. The net influence of these two interacting effects is highlighted by plotting the non-dimensionalised pressure (P/P_G) as shown in Fig. 14 and 15. By comparing the lines of the 3 µm case for 0 rpm (hydrostatic pressure), 10380 rpm and 30000 rpm, it is evident that for 10380 rpm no significant centrifugal effect exists. However at 30000 rpm, a notable change in the pressure profile is observed. The results are in agreement with previous theoretical work by Garratt [31], who identified that rotation leads to a reduction in radial mass flow

and pressure across the seal. Consequently, these effects influence on the performance parameters of the seal, such as opening force and total mass flow rate.

As shown in Fig. 14 and Fig. 15, the centrifugal effect (reduction of pressure) increases as the rotational speed increases and as the film gap decrease. Furthermore the results show that the centrifugal effect is more significant for CO_2, especially at low gaps and high rotation speeds and that it is strongest for CO_2 close to critical point. This is due to the higher gas densities for CO_2 (see inlet density in Table 2), which further increases if higher peak pressures are reached at the end of the groove, for example as shown in Fig. 5a and 9a.

Effectively this means that the centrifugal effects are strongest at high speeds, high fluid densities as is the case with CO_2, and that high peak pressures reached at the end of the grooves further enhance the effect. The impact of centrifugal effects on seal performance are: First increased centrifugal effects lead to a reduction in avergage pressure (i.e. mainly due to reduction of pressure in the dam region) and thus reduced opening force. Second increased centrifugal effects lead to comparably reduced leakage (i.e. by increasing outward force acting on fluid). However at the same time this causes higher peak pressures (i.e. due to the lower leakage) at the end of the groove which tend to increase leakage (i.e. flow to the lower pressure region). The net effect on seal opreation is explored with the different air and supercritical CO_2 seal simulations.

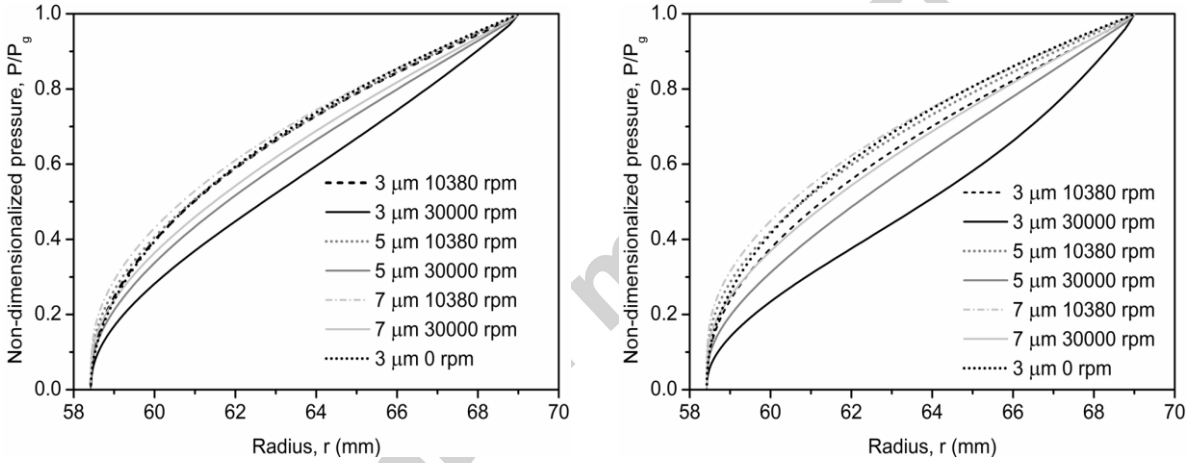

a) Air (ideal gas equation of state) b) CO_2 (Span and Wagner equation of state)

Fig. 14. Non-dimensionalized pressure across the dam region at T = 370 K.

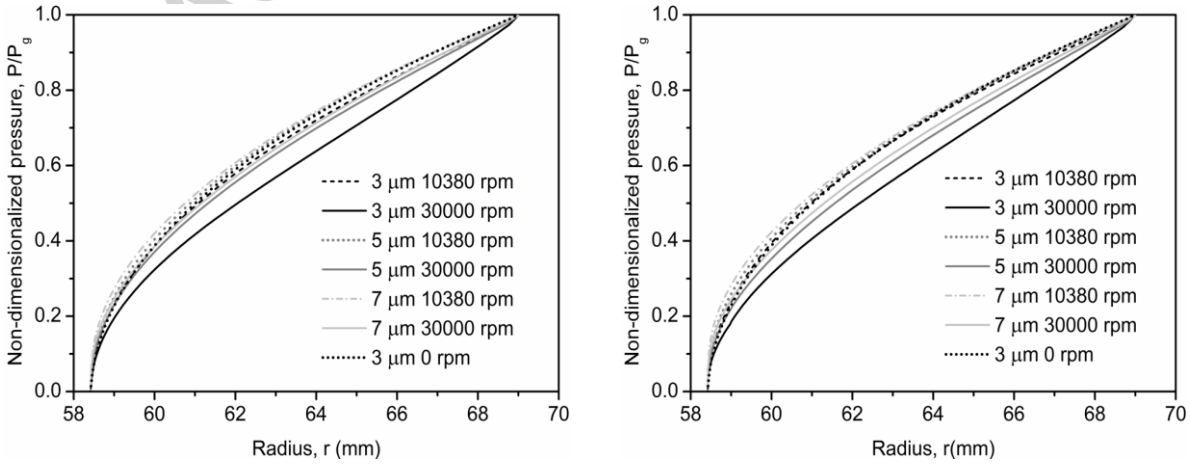

a) Air (ideal gas equation of state) b) CO_2 (Span and Wagner equation of state)

Fig. 15. Non-dimensionalized pressure across the dam region at T = 740 K.

3.2.2 Pressure profiles and contours

Fig. 16 shows the pressure distribution in the radial direction for air and CO_2 for a 3.05 μm film gap, which experience the strongest viscous effects due to the small gap height. Due to viscous pumping in the groove region (r > 69 mm) the pressure increases from the outer edge until the end of the groove where the peak pressures are reached. Particularly high pressures are reached at a rotational speed of 30000 rpm. Fig. 17 shows the corresponding pressure contours for CO_2 at a rotational speed of 30000 rpm, which highlights that the peak pressures are localised to the end of the goove. After the grooves, in the dam region (r < 69 mm) the pressure decreases to ambient conditions (0.1 MPa) at the inner edge of the seal.

When operating with air the pressure profiles are almost identical to the ones observed with CO_2 at an operating temperature of 740 K, confirming the similarity between hot CO_2 and ideal gases. For air the effect of increasing temperature is small at the high rotational speeds. The only difference in pressure contours exists close to the end of the dam region. At low rotation speed as tempereture increases, the pressure increases due to the increase of viscosity with temperature, which increases viscous pumping in the grooves for the 740 K case.

As expected, as rotational speed increases more gas is pumped inward thereby resulting in higher presures developing at the end of the groove. This has the following effects. First the high pressures cause some backwards flow towards seal outer edge in the regions between the grooves (i.e. to lower pressure region) and second the associated higher densities enhance the sealing performance of the dam as discussed previously. A downside of the second effect, particulalry with the higher densities reached at lower temperatures (370 K) is that the increased centrifugal forces, caused by tangential fluid motion, resist the inwards flow. This results in a reduction of pressure across the seal dam, as observed for the 30000 rpm case.

The overall patterns are similar for the CO_2 (Fig. 16b) except for the 370 K, 30000 rpm case, where pressures at the end of the groove are substantially higher compared to air. To understand this phenomenon, the balance of mass-flow between the fluid entering the groove and the flow leaving the groove toward the dam region must be considered. This mass-flow balance directly influences the peak pressure developed in the groove. Effectively strong inwards pumping by the groove and good sealing by the dam is required to create such high pressures. Looking back at Fig. 14b it is evident that this case also experienced the strongest centrifugal effects. Hence, here the centrifugal effect, which increases with density is able to balance the strong pumping effect of the grooves. Consequently, much higher peak pressures are attained as the leakage from the grooves to the dam is reduced.

A somewhat counter-intuitive result is that this only occurs for CO_2 and not for air. As can be seen from Fig. 14 and 15 the effect of changing temperature on pressure inside the sealing dam for air is minor compared to CO_2. The larger changes for CO_2 are due to the different equations of state and different fluid properties close to the critical point. As previously shown in Fig. 9a the use of the real gas equation Eq. (7) instead of Eq.(6) results in a more rapid change in fluid density at the seal centre (near the end of the groove). Therefore, this higher localised density that exists for CO_2 is the cause for the difference in pressure distribution observed for CO_2. This localised density change at the end of the groove is not observed for the ideal gas model as shown in Fig. 8a and 9a and hence not for air (Fig.

8b and 9b) .

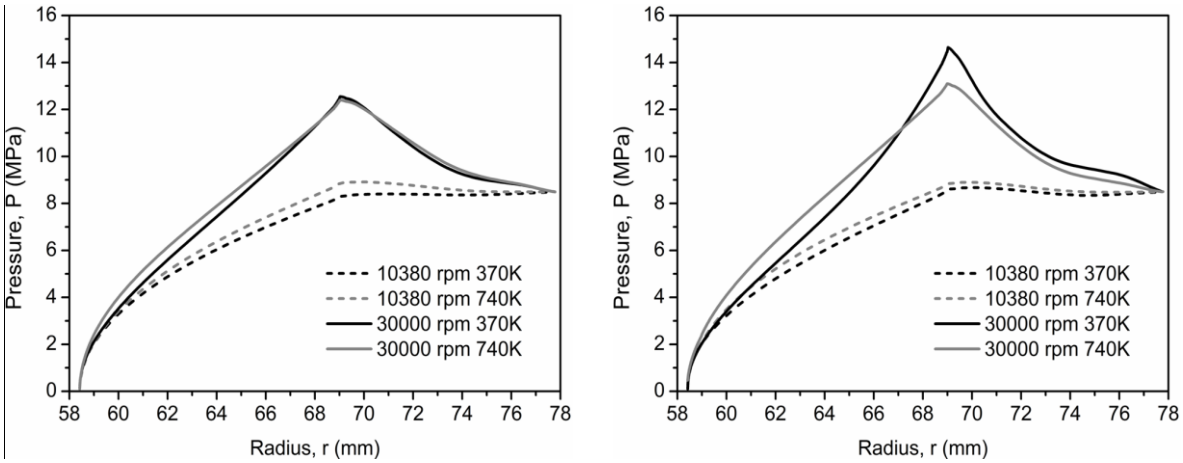

a) Air (ideal gas equation of state) b) CO_2 (Span and Wagner equation of state)

Fig. 16. Pressure distribution for ideal and real gas in radial direction, h = 3.05 µm.

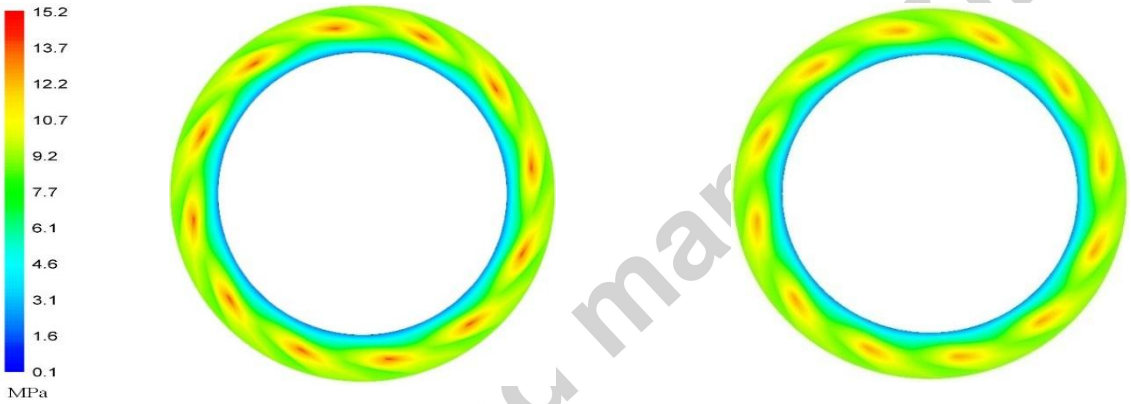

a) T =370 K b) T =740 K

Fig. 17. Pressure contours for CO_2, ω = 30000 rpm and h = 3.05 µm.

As film gap increases to 5.08 µm for air (Fig. 18a) similar pressure profiles are observed compared to the lower gap. However the pressures reached at the end of the grooves are lower and the effect of temperature has disappeared. This is attributed to the reduction in viscous pumping as the film gap increases [28] and the diminishing performance of the sealing dam to resist inwards flow. At 30000 rpm a pressure increase in the grooves is still noticable and this is also shown in the corresponding pressure contours (Fig. 19). However at the low speed (10380 rpm) the viscous pumping is so weak that pressure smoothly decreases from the outer to the inner radius of the seal.

For CO_2 (Fig. 18b), the patterns also remain similar, however the peak pressure reached at the end of the groove is reduced. The difference in peak pressure that arises at the end of the grooved due to the nonlinear fluid properties that exist for the cold CO_2 near the critical point remain at the high speed, albeit to a lesser extend. At 10380 rpm the pressure profiles are more or less identical. Effectively with the higher gap the centrifugal effect and hence the performance of the sealing dam is reduced, thereby leading to reduced peak pressures at the groove end and more uniform pressures as shown in Fig. 19b.

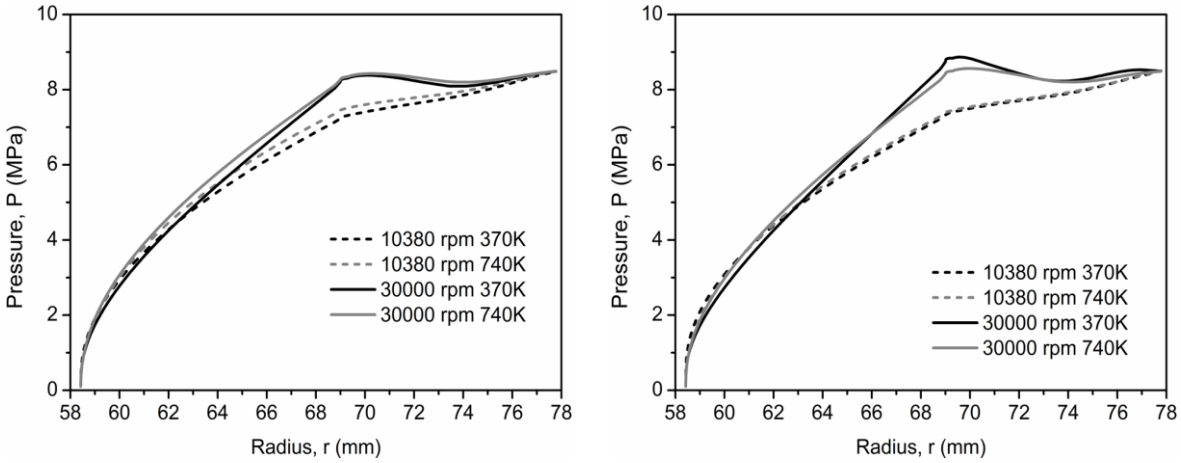

a) Air (ideal gas equation of state) b) CO_2 (Span and Wagner equation of state)

Fig. 18. Pressure distribution for ideal and real gas in radial direction, h = 5.08 µm.

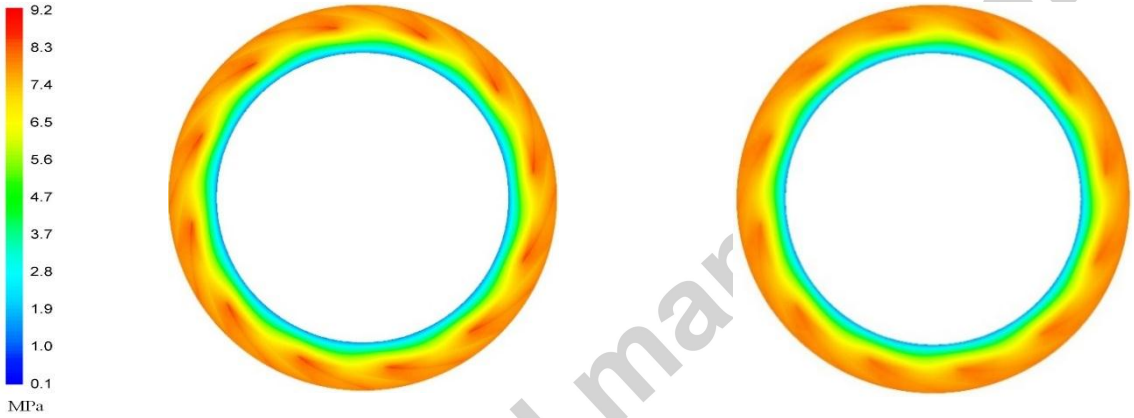

a) T = 370 K b) T = 740 K

Fig. 19. Pressure contours for CO_2, ω = 30000 rpm and h = 5.08 µm.

The results for the largest gap of 7 µm for air and CO_2 are shown in Fig. 20. As both the pumping efficiency of the grooves and centrifugal effects that enhance sealing dam performance are further reduce, the pressure distribution is comparable for all cases. It decreases from outer radius to inner radius of the seal domain. Similarly no significant pressure increases are observed at the end of the grooves as shown in Fig. 21.

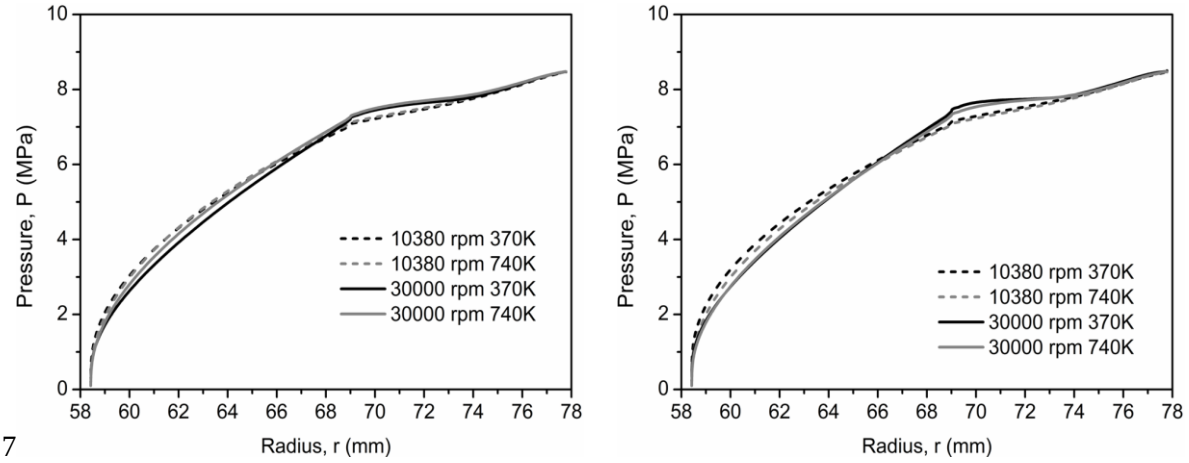

a) Air (ideal gas equation of state) b) CO_2 (Span and Wagner equation of state)

Fig. 20. Pressure distribution for ideal and real gas in radial direction, h = 7 µm.

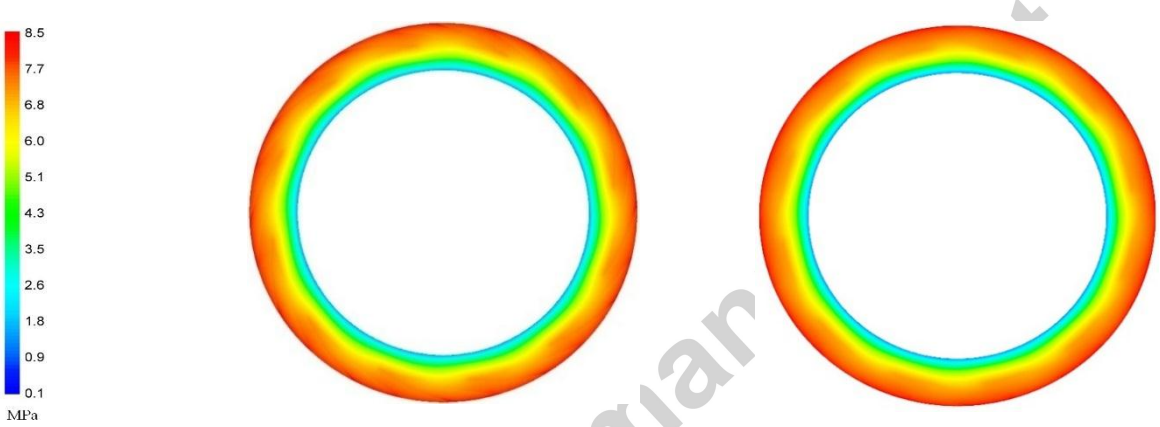

a) T =370 K b) T =740 K

Fig. 21. Pressure contours for CO_2, ω = 30000 rpm and h = 7 µm.
(air results are comparable to 740K case)

To summarise, effectively as gap heigth increases viscous effect, such as the pumping efficiency of the grooves and inertial effects, such as the centrifgual force that enhances sealing dam performance diminishes. Consequently differences between the air (lower density ideal gas) and CO_2 (higher density gas with real gas effects) dissappear and the air and CO_2 seal behave equivalently. However with small gaps different pressure distributions are observed. These are due to two factors. First the CO_2 is more dense, leading to an increased centrifugal force that improves sealing dam performance. Second the non-linear gas properties of the CO_2 near the critical point cause a more rapid density change and hence increased centrifugal force at the start of the sealing dam. This further enhances seal performance as it enables the generation of higher peak pressures in the grooves.

3.2.4 Opening force

Fig. 22 shows the opening force at different operating temperatures, rotation speeds and film thickness for air and CO_2 respectively. As expected due to the reduced pumping effect as the film gap increases the opening force decrease and asymptotes towards a constant value. At a rotational speed of 10380 rpm and 370 K, the condition where the viscous effects are smallest the steady value is reached for both air and CO_2 at gaps larger than 5µm. The high opening forces with small film thicknesses are

created by the fact that here the pumping of the grooves is strongest and that the dam creates the best flow obstruction. These effects together create high peak pressures, which yield the biggest net opening forces. Overall the observed trends for air and CO_2 are similar.

When considering the effect of rotational speed, while keeping temperature constant, it is observed that at low gap heights (< 5 μm) the higher speed creates the higher opening forces. This is expected as higher speeds create increased viscous pumping. However for high gap heights (> = 6 μm) this trend is reversed. This can be attributed to the lower pressures in the dam region as shown in Fig. 16a, 18a and 20a, which are caused by the centrifugal force that causes a reduction of pressure in the sealing dam at high rotational speeds.

When considering the effect of temperature, while keeping rotation speed constant, it is observed that for air this creates a notable offset in opening force (approx. 1.0 – 2.0 kN). At a rotational speed of 10380 rpm as tempereture increases, the viscous pumping in the grooves increases due to the increase of viscosity with temperature. At high rotational speed, this effect is slightly enhanced due to the different pressure distributions in the dam region (e.g. Fig. 14a and 15a). Here higher pressures are created for the less dense air at 740 K.

For CO_2, the effect of temperature is much reduced, especially at the high rotational speed across all gap heights. This is due to the fact that for CO_2, two effects interact. First as observed for air, the pressure across the dam is lower for the high temperature (see Fig. 16b and 17b). Second notably different peak pressures are created at the end of the groove, for example as shown in Fig. 16b, 17b, 18b, 19b. As these effects approximately balance, the dependency of opening force on temperature is reduced for CO_2, particularly at high rotational speed.

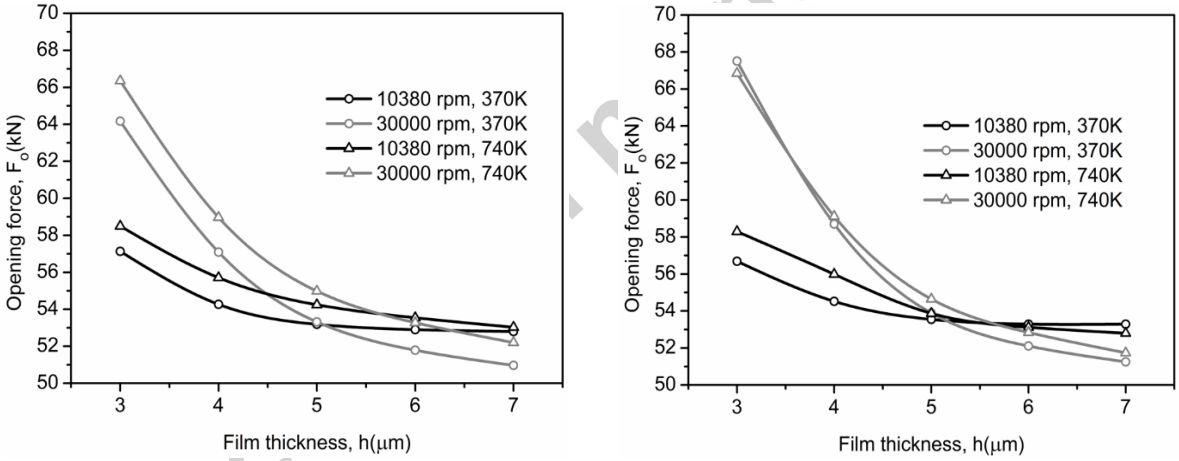

a)Air (ideal gas equation of state) b) CO_2 (Span and Wagner equation of state)

Fig. 22. Opening force, F_o at different rotation speed and film gap for ideal and real gas.

3.2.5 Leakage rate

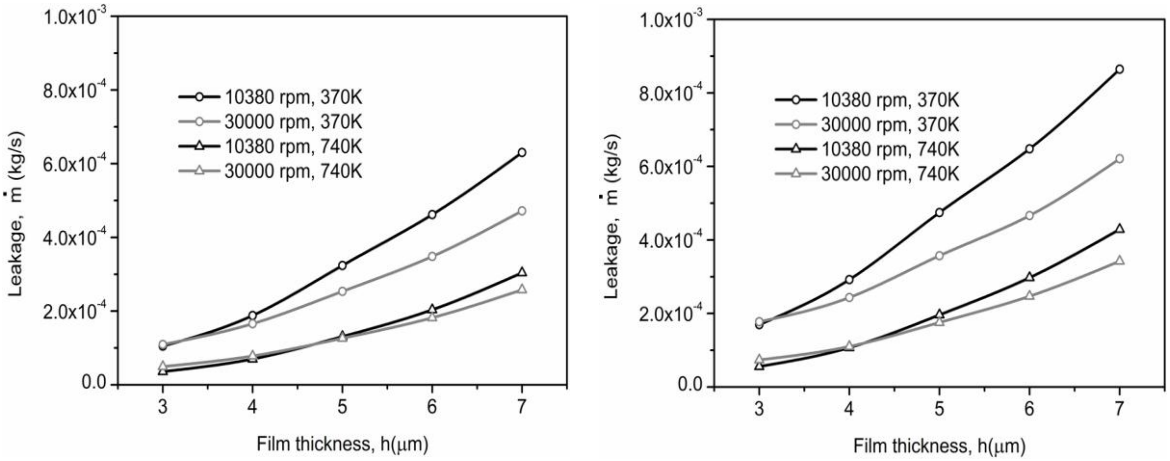

a) Air (ideal gas equation of state) b) CO_2 (Span and Wagner equation of state)

Fig. 23. Mass flow rate, ṁ at different rotation speed and film gap for ideal and real gas.

Fig. 23 shows the leakage rate for air and CO_2. For all cases, it is shown that as the film gap increases, which is equivalent to an increase in total flow area, so does the leakage rate. In addition leakage rates are also strongly influences by temperature, which inversely correlates to density. The strong link between density and mass flow rate indicates the importance of density on seal performance.

For high temperature case (triangular symbol) as shown in Fig. 23, the leakage rate is almost the same for the two rotational speeds at low film gap (< 4 μm) . However, as the film gap increases (> 5 μm) the leakage increases more rapidly the for rotational speed of 10380 rpm in comparison with 30000 rpm. This is the result of reduced inward pumping in the groove region as the film gap increases and the increase of the outward pumping effect as rotational speed increases. The outward pumping effect is as a result of the stronger centrifugal effect as rotational speed increases.

For the low temperature case (circular symbols), the overall trend for both speeds and gases is again similar. However now a notable discrepancy between low speed and the high speed is observed. For both air and CO_2 leakage reduces by more than 20% as rotational speed increases to 30000 rpm, for the largest gap. However for low gap heights (< 4μm) the leakage is comparable. This is the result of two opposing effects caused by the high density and real gas effects. First the high density and real gas effects enhance the performance of the sealing dam and the grooves, resulting in higher peak pressures at the groove ends as shown in Fig. 16 and 18. However these increases in pressure differential across the dam also increase leakage. The result is that the actual leakage from the grooves towards the seal outlet increases. As this change approximately balances with the centrifugal effect, which decreases leakage, comparable results are observed for the denser gas (lower temperature). The bigger change for CO_2 is attributed the real gas effect that is present at the end of the groove discussed earlier.

4. Conclusions

To enhance the understanding of dry gas seals operating with CO_2 at supercritical conditions a numerical study was conducted. First the numerical model was validated for operation with air by comparing predictions to experimental results from literature. Good agreement was achieved with errors in groove pressure of less than 0.3% and opening force of less than 6 %.

Next to quantify real gas effects that affect CO_2 thermal and transport properties near the critical

point, a comparison study was performed. The ideal gas equation of state and Span and Wagner equations of state (incorporating real gas effects) were compared at T = 370 K near the critical point and at 740 K far from critical point. Comparison of the resulting fluid properties and seal performance parameters indicate that close to critical point the real gas effect is significant whereas far from critical point (i.e. at T = 740 K) the supercitical fluid resembles an ideal gas. The main differences in performance arises in the seal grooves and at the end of the sealing dam closest to the grooves. Here a more rapid change in gas density enhances performance. Hence when simulating seals operation far from the critical point it is acceptable to use the ideal gas relationshiop. However when the operating point is close to the critical point, real gas effects are significant and an appropriate equation of state is required to correctly capture the fluid dynamics, particularly at the end of the grooves.

Finally the paper conducts a study comparing the same seal geometry operating with air and CO_2 at four operating points. (P_i = 8.5 MPa, ω = 10380 and 30000 rpm, T_i = 370 and 740 K). This provides insight into how seal operation is affected by the denser CO_2, the real gas effects and the resulting centrifugal effects that influence the operation of the sealing dam. In the dam region of the seal the centrifugal effect has two effects. First it improves sealing by creating a higher peak pressures at the end of the groove. Second it reduces the average pressure within the dam region due to improved sealing at the dam outer diameter. The second effect is enhanced for CO_2 due to real gas effects. The net effect of this is a reduction of the opening force at high rotation speed, where the centrifugal effect is most significant. Comparing the impact of these two effects on seal performance it can be seen that the seal leakage reduction is most significant and beneficial. Especially at high operating gaps it can lead to a leakage reduction of more than 20%.

In general it has been shown that operation with supercritical CO_2 close to critical point (P_i = 8.5 MPa, T_i = 370 K) is not detrimental to seal performance. The opening force is comparable to that of an equivalent seal operating with ideal gases. Seal leakage remains similar, but scales with inlet density. At low gap heights equivalent leakages are observed. However at high rotational speeds a notable leakage reduction exists due to a combination of centrifugal and real gas effects.

Future works will investigate the effects of conjugate heat transfer and thermal deformation of the seal components. This will provide further insight required for the developement of supercitical CO_2 dry gas seals.

Acknowledgement

This research is part of the Australian Solar Thermal Research Initiative (ASTRI) a project support by the Australian government. The first author would also like to thank the University of Queensland and Malaysian government for financial support.

References

[1] Stahley JS. Dry gas seals handbook. PennWell; 2005.
[2] Forsthoffer WE. Forsthoffer's Best Practice Handbook for Rotating Machinery. Butterworth Heinemann; 2011.
[3] Song P, Chen K, Dong Z. A theoretical analysis of spiral groove upstream pumping mechanical seal. Lubrication and Seal 1999; 24: 5-7.
[4] Bing W, Huiqiang Z, Hongjun C. Flow dynamic of spiral groove dry gas seal. Chinese Journal of Mechanical Engineering 2013; 26(1):78-84.
[5] Bonneau D, Huitric J, Tournerie B. Finite element analysis of grooved gas thrust bearings and grooved gas face seals. ASME Journal of Tribology 1993;115:348–54.

[6] Hong W, Baoshan Z, Jianshu L, Changliu Y. Thermohydrodynamic analysis of dry gas seals for high-temperature gas cooled reactor. Journal of Tribology 2012; 135(2): 021701- 021709.

[7] Vhor JH, Pan CHT. On the spiral grooved self-acting gas-bearing. Office of Naval Research 1964; MTI Report No. 63TR52.

[8] Heshun W, Weibing Z. and Qiang W. Numerical simulation on flow field of spiral grooved dry gas seal. In: International Conference on Computer Design and Application 2010; 5:227-230.

[9] Thatte A, Zheng. X. Hydrodynamics and sonic flow transition in dry gas seals. In: Proceeding of ASME Turbo Expo. Turbine Technical Conference and Exposition Germany 2014; GT2014-26706.

[10] Shahin I, Gadala M, Alqaradawi M. and Badr O. Centrifugal compressor spiral dry gas seal simulation working at reverse rotation, In: The Malaysian International Tribology Conference Procedia Engineering 2013; 68: 285–292.

[11] Shahin I, Gadala M , Alqaradawia M, Badr O. Three dimensional computational study for spiral dry gas seal with constant groove depth and different tapered grooves. In: The Malaysian International Tribology Conference Proceeding Engineering 2013: 68: 205–212.

[12] Marquartdt JT. Successful operation experiences sealing supercritical CO_2. In: Supercritical CO_2 Power Cycle Symposium 2011 ; 24-25. Boulder Colorado.

[13] Muijderman E.A. Spiral groove bearing, Industrial Lubrication and Tribology 1965; 17(1):12-17

[14] Malanoski S.B, Pan C.H.T. The static and dynamic characteristics of the spiral-grooved thrust bearing. ASME Journal of Basic Engineering 1965: 87:547–558.

[15] Smalley A.J. The narrow groove theory of spiral groove gas bearing. Development and application of a generalized formulation for numerical solution. ASME Journal of Lubrication Technology 1972; 94: 86–92.

[16] James DD, Potter AF. Numerical analysis of the gas lubricated spiral-groove thrust bearing-compressor. ASME Journal Lubrication Technology 1967: 91(4): 439–444.

[17] Qin K, Jahn I, Gollan R, Jacobs P. Development of a computational tool to simulate foil bearings for supercritical CO2 cycles. Submitted to Computers and Fluids.

[18] M.F.Zakariya, Ingo H.J. Jahn, Performances of supercritical CO_2 dry gas seal near critical point. In: Proceeding of ASME Turbo Expo 2016: Turbomachinery Technical Conferences & Exposition 2016.

[19] Jing X, Xudong P, Shaxian B, Xiangkai M. CFD simulation of microscale flow field in spiral groove dry gas seal. In: Mechatronics and Embedded Systems and Applications IEEE/ASME International Conference 2012.

[20] Kimball KJ, Clementoni MEM. Supercritical carbon dioxide Brayton power cycle development overview. In: Proceedings of ASME Turbo Expo 2012.

[21] Wright SA, Radel RF, Vernon ME, Rochau GE and Pickard PS. Operation and analysis of a supercritical CO_2 Brayton cycle 2010: Sandia Report SAND2010-0171.

[22] Clifford T, Fundamental of supercritical fluids. Oxford University Press, Inc., New York;1999.

[23] Ansys Inc. Ansys FLUENT User Guide Release 16 ; 2015.

[24] Span R, Wagner W. A new equation of state for carbon dioxide covering the fluid region from triple point temperature to 1100K at pressure up to 800 MPa. Journal of Physical and Chemistry Reference Data 1996; 25:1509-1596.

[25] Linstrom PJ, Mallard WG. NIST Chemistry Webbook, NIST Standard References Database Number 69. National Institute of Standards and Technology, Gaitersburg MD, 20899. http://webbook.nist.gov/chemistry/

[26] Brunetiere N, Tournerie B and Frene J. Influence of fluid flow regimes on performances of non-contacting liquid face seals. ASME Journal of Tribology 2002; 124(3): 515-523.

[27] Baltadjiev ND. An investigation of real gas effects in supercritical CO_2 compressors. Master of Science Thesis. Massachusetts Institute of Technology; 2012.

[28] Gabriel RP. Fundamentals of spiral groove non-contacting face seals. Lubrication Engineering 1994; 50(3): 215-224.
[29] Jacobs PA, Gollan RJ, Jahn I, Potter DF. The Eilmer3 Code: User guide and example book ; 2015 Edition.
[30] Jahn I, Qin K. e3prepToFoam: a mesh generator for OpenFOAM, Mechanical Engineering Technical Report 2015/04; May 2015.
[31] Garratt JE, Hibberd S, Cliffe KA. Centrifugal inertia effects in high speed hydrostatic air thrust bearing, Journal of Engineering Mathematics 2012; 76 (1): 59-80.

Appendices

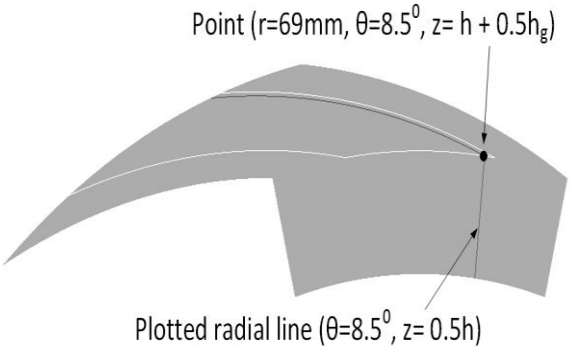

Appendix 1: Point and line of interest for the present work.

Highlight

The contributions of the present paper as follows:

i) provide some design guidelines by providing some insight on the flow behaviour on the performance of the supercritical fluid (i.e. CO_2) of the dry gas seal.
ii) study the flow behaviour on the performance of the supercritical dry gas seal at two possible operating conditions; one is close and another is far from critical point.
iii) provide some insight on impact of centrifugal effect on the performance of the supercritical dry gas seal which is rarely studied even for ideal gas fluid.

The important findings of the present paper as follows:

i) fluid properties and seal performance parameters indicate that close to critical point the real gas effect is significant whereas far from critical point the supercitical fluid resembles an ideal gas.
ii) the centrifugal effect cause both improved sealing in the dam region due to real gas effects, generating a higher peak pressures at the end of the grooves and a reduction of average pressure due to improved sealing at the dam outer diameter. However, the net effect is a reduction of the opening force at high rotation speed where the centrifugal effect is most significant.
iii) the centrifugal effect also reduces seal leakage, which is beneficial for seal performance.

iv) operation with supercritical CO_2 close to critical point is not detrimental to seal performance.